Methods for direct simulation of transition in hypersonic boundary layers

By J. J. W. van der Vegt AND J. H. Ferziger

An implicit numerical algorithm for the time accurate solution of the compressible Navier-Stokes equations is described. Results for steady flow past a finite flat plate are presented, together with preliminary results for the temporal simulation of second mode instability in a flat plate boundary layer at Mach 4.5.

1. Motivation and objective

The proposed new generation of supersonic and hypersonic vehicles pose tremendous challenges to prediction methods for high speed flows. Transition to turbulence is crucial to the design of these vehicles but is far from completely understood. Direct simulations can complement experiments by offering opportunities to study cases which are very difficult or impossible to realize experimentally. This report discusses numerical methods for direct simulation of transition in boundary layers. We have developed and improved a time-accurate numerical method for flows with both strong shocks and boundary layers; for more details see van der Vegt (1991). Efficient ways to obtain steady state solutions, needed as initial conditions, have been implemented. Calculations of the temporal stability of the second mode in a flat plate boundary layer have been started; the main objective is to study the effects of wall temperature on stability.

2. Accomplishments

The main activities in 1990 have been the further development of a time accurate method for the Navier-Stokes equations; a start has been made on transition calculations on a flat plate. The requirements of time accuracy and rapid convergence to a steady state are partially conflicting because one can improve convergence by adding dissipation while one tries to minimize dissipation in time-accurate calculations. Whenever there is conflict between these requirements, time accuracy is favored. Strong shocks and boundary layers present different problems. It was decided to develop a fully implicit method because the equations are stiff, resulting in an impractical time step limitation for explicit methods.

An implicit method is, however, more complicated than an explicit method. There are a number of implicit methods available for the compressible Navier-Stokes equations. One of the most widely used methods is that of Beam and Warming (1978), which is not well suited for our problem. For time-accurate solutions, the approximate factorization adds an additional error and the viscous cross-coupling terms cannot be factorized. In addition, the use of central differences requires artificial viscosity to obtain stable solutions when there are shocks. The Beam-Warming

method obtains steady state solutions efficiently but is not well suited to time-accurate calculations.

An alternative is to choose one of the modern upwind methods developed for the Euler equations such as flux splitting according to Steger and Warming or van Leer, approximate Riemann solvers, and TVD methods; for a review see Vinokur (1989). These methods all incorporate some properties of the Euler equations and accurately compute shocks without explicit artificial dissipation. We chose Steger-Warming splitting in which the components related to the positive and negative eigenvalues of the operator are treated differently. The method accounts for information travel along the (inviscid) characteristics. At high Reynolds number, this is nearly correct in most of the flow. Flux splitting for the non-linear terms has an additional beneficial effect; it yields a diagonally dominant matrix well suited to iterative solution. In the viscous region, however, flux splitting can produce unwanted numerical dissipation, as was demonstrated by MacCormack and Candler (1989). The correction to the Steger-Warming splitting proposed by MacCormack was adopted and modified for the boundary layer, whereas the Steger-Warming splitting, described in Steger and Warming (1981), is used in a shock. The diagonal dominance of the matrix allows iterative solution and all the viscous components to be treated implicitly. It also gives more freedom in the choice of boundary conditions.

Numerical Method

A finite-volume method is used because an integral formulation is conservative and better suited to flows with shocks. The present algorithm solves the two-dimensional compressible Navier-Stokes equations in conservation form in an arbitrary coordinate system. These can be written:

$$\frac{\partial}{\partial t}\hat{\mathbf{U}} + \frac{\partial}{\partial \xi}(\hat{\mathbf{E}} - \hat{\mathbf{V}}_{vis_\xi}) + \frac{\partial}{\partial \eta}(\hat{\mathbf{G}} - \hat{\mathbf{V}}_{vis_\eta}) = \mathbf{0} \tag{1}$$

with:

$$\hat{\mathbf{U}} = \frac{\mathbf{U}}{J}; \quad \hat{\mathbf{E}} = \frac{\xi_x}{J}\mathbf{E} + \frac{\xi_z}{J}\mathbf{G}; \quad ,\hat{\mathbf{G}} = \frac{\eta_x}{J}\mathbf{E} + \frac{\eta_z}{J}\mathbf{G}$$

$$\hat{\mathbf{V}}_{vis_\xi} = \frac{\xi_x}{J}\mathbf{V} + \frac{\xi_z}{J}\mathbf{I}; \quad \hat{\mathbf{V}}_{vis_\eta} = \frac{\eta_x}{J}\mathbf{V} + \frac{\eta_z}{J}\mathbf{I}$$

and:

$$\mathbf{U} = \begin{pmatrix} \rho \\ \rho u \\ \rho w \\ e \end{pmatrix}; \quad \mathbf{E} = \begin{pmatrix} \rho u \\ \rho u^2 + p \\ \rho uw \\ (e+p)u \end{pmatrix}; \quad \mathbf{G} = \begin{pmatrix} \rho w \\ \rho uw \\ \rho w^2 + p \\ (e+p)w \end{pmatrix}$$

$$\mathbf{V} = \frac{1}{Re}\begin{pmatrix} 0 \\ \tau_{xx} \\ \tau_{xz} \\ u\tau_{xx} + w\tau_{xz} - \frac{q_x}{(\gamma-1)M^2 Pr} \end{pmatrix}; \; \mathbf{I} = \frac{1}{Re}\begin{pmatrix} 0 \\ \tau_{xz} \\ \tau_{zz} \\ u\tau_{xz} + w\tau_{zz} - \frac{q_z}{(\gamma-1)M^2 Pr} \end{pmatrix}$$

$$\tau_{xx} = (2\mu + \lambda)\frac{\partial u}{\partial x} + \lambda\frac{\partial w}{\partial z}; \quad \tau_{xz} = \mu(\frac{\partial u}{\partial z} + \frac{\partial w}{\partial x}); \quad \tau_{zz} = (2\mu + \lambda)\frac{\partial w}{\partial z} + \lambda\frac{\partial u}{\partial x}$$

$$q_x = -\kappa\frac{\partial T}{\partial x}; \quad q_z = -\kappa\frac{\partial T}{\partial z}$$

The equation of state is: $p = \frac{\rho c_v T}{\gamma M^2}$

Here ρ represents the density, u and w the velocity components in a Cartesian coordinate system, p the pressure, T temperature, and e the total energy. The variables x and y represent Cartesian coordinates, whereas ξ and η represent curvilinear coordinates. The coefficients M and Pr are the Mach and Prandtl numbers, while μ, λ, and κ are the two viscosities and thermal conductivity. The shear stress and heat flux components in $\mathbf{V}$ and $\mathbf{I}$ are functions of ξ and η. All variables are non-dimensionalized using free-stream variables and a characteristic length. Use of a general coordinate system adds flexibility but greatly increases the complexity of the code.

The numerical scheme will now be summarized. The first step is the choice of a time integration method. The time integration is formulated as a Padé relation, cf. Beam and Warming (1978):

$$\Delta\hat{\mathbf{U}}^n = \frac{\alpha\Delta t}{1+\beta}\frac{\partial}{\partial t}\Delta\hat{\mathbf{U}}^n + \frac{\Delta t}{1+\beta}\frac{\partial}{\partial t}\hat{\mathbf{U}}^n + \frac{\beta}{1+\beta}\hat{\mathbf{U}}^{n-1} + O[(\alpha - \tfrac{1}{2} - \beta)\Delta t^2 + \Delta t^3]$$

with: $\Delta\hat{\mathbf{U}}^n = \hat{\mathbf{U}}^{n+1} - \hat{\mathbf{U}}^n$

The coefficients α and β allow different time integration schemes to be obtained. For instance, $\alpha = 1$, $\beta = 0$ give the implicit Euler method, $\alpha = .5$, $\beta = 0$ give the trapezoid rule, and $\alpha = 1$, $\beta = 0.5$ give a three point backward scheme. The superscript n refers to time $t = t_n$.

Introducing the compressible Navier-Stokes equations (1) into this relation yields:

$$\begin{aligned}\Delta\hat{\mathbf{U}}^n =& \frac{\alpha\Delta t}{1+\beta}\{-\frac{\partial}{\partial\xi}(\Delta\hat{\mathbf{E}}^n - \Delta\hat{\mathbf{V}}^n_{vis_\xi}) - \frac{\partial}{\partial\eta}(\Delta\hat{\mathbf{G}}^n - \Delta\hat{\mathbf{V}}^n_{vis_\eta})\}+ \\ & \frac{\Delta t}{1+\beta}\{-\frac{\partial}{\partial\xi}(\hat{\mathbf{E}}^n - \hat{\mathbf{V}}^n_{vis_\xi}) - \frac{\partial}{\partial\eta}(\hat{\mathbf{G}}^n - \hat{\mathbf{V}}^n_{vis_\eta})\} + \frac{\beta}{1+\beta}\Delta\hat{\mathbf{U}}^{n-1}\end{aligned} \tag{2}$$

which is first or second order accurate in time, depending on the choice of α and β.

Applying Gauss' theorem and integrating equation (2) over a small volume gives the finite-volume formulation for the compressible Navier-Stokes equations:

$$\begin{aligned}\Delta\overline{\mathbf{U}}_{i,j} =& \frac{\alpha\Delta t}{1+\beta}\{-\Delta\overline{\mathbf{G}}^n_{i,j-\frac{1}{2}} + \Delta\overline{\mathbf{E}}^n_{i+\frac{1}{2},j} + \Delta\overline{\mathbf{G}}^n_{i,j+\frac{1}{2}} - \Delta\overline{\mathbf{E}}^n_{i-\frac{1}{2},j}\}+ \\ & \frac{\Delta t}{1+\beta}\{-\overline{\mathbf{G}}^n_{i,j-\frac{1}{2}} + \overline{\mathbf{E}}^n_{i+\frac{1}{2},j} + \overline{\mathbf{G}}^n_{i,j+\frac{1}{2}} - \overline{\mathbf{E}}^n_{i-\frac{1}{2},j}\} + \frac{\beta}{1+\beta}\Delta\overline{\mathbf{U}}^{n-1}\end{aligned} \tag{3}$$

where a barred quantity with index i,j is an average of the unbarred quantity over the cell with index i,j and indices $i \pm \frac{1}{2}$ and $j \pm \frac{1}{2}$ refer to values at the cell faces.

Flux Vector Splitting

Flux vector splitting is powerful for computing flows with strong shocks. Upwind methods are, however, dissipative. Dissipation is necessary in shocks but not in smooth flows such as boundary layers. MacCormack and Candler (1989) presented a way to improve the accuracy of flux vector splitting significantly in regions outside shocks. This method, in modified form, is discussed in this section.

The Steger-Warming splitting is based on the homogeneity property of the Euler equations:

$$\hat{\mathbf{E}}^n(\mathbf{U}) = \left(\frac{\partial \hat{\mathbf{E}}^n}{\partial \mathbf{U}}\right)\mathbf{U}^n = S^{-1}C^{-1}\Lambda C S\mathbf{U}$$

with : $S = \frac{\partial \mathbf{U}}{\partial \mathbf{V}}$, where $\mathbf{V} = (\rho, u, v, p)^T$, C is related to the metrics, density and speed of sound a, and $\Lambda = (u, u, u+a, u-a)^T$, the eigenvalue matrix.

In the Steger-Warming approach, the flux vector is split in vectors $\hat{\mathbf{E}}^{\pm}$ by separating the matrix Λ in matrices with positive and negative eigenvalues. As demonstrated by MacCormack and Candler (1989), this gives a dissipative approximation to the flux at the cell surface when using a finite-volume method. They demonstrated that for the incompressible flat plate boundary layer, it is much better to approximate the Jacobian matrix $\frac{\partial \hat{\mathbf{E}}^n}{\partial \mathbf{U}}$ at the surface $i+\frac{1}{2}$ by alternately using its value at i and $i+1$ for the components related to the momentum equations. This method was tested in great detail, but like the explicit predictor-corrector MacCormack scheme, it has the disadvantage that the error is oscillatory and depends on the time step, so the computation never reaches completely a steady state. Also, the location at which the metrics of the coordinate transformation are computed is not clear in their paper. In their finite-volume formulation of the Steger-Warming splitting, they use the metrics at the cell center, while the metrics at the cell faces should be used. This requires four times as many computations of the metrics, but it pays off in terms of accuracy.

The modified MacCormack splitting can now be defined in terms of:

$$D = \mathrm{diag}(\alpha_1, \alpha_2, \alpha_3, \alpha_4)$$

$$\tilde{S}_{i+\frac{1}{2}} = DS_i + (I - D)S_{i+1}$$

Similar expressions define $\tilde{C}_{i+\frac{1}{2}}$ and $\tilde{\Lambda}_{i+\frac{1}{2}}$. Here I represents the identity matrix and D a diagonal matrix. The modified flux is defined as:

$$\hat{\mathbf{E}}^{+}_{i+\frac{1}{2}} = \tilde{S}^{-1}_{i+\frac{1}{2}}\tilde{C}^{-1}_{i+\frac{1}{2}}\tilde{\Lambda}_{i+\frac{1}{2}}\tilde{C}_{i+\frac{1}{2}}\tilde{S}_{i+\frac{1}{2}}\mathbf{U}_i$$

with an equivalent relation for $\hat{\mathbf{E}}^{-}_{i+\frac{1}{2}}$, with $\mathbf{U}_i$ replaced by $\mathbf{U}_{i+1}$.

The main difference between the splitting presented in MacCormack and Candler (1989) and the one used in this paper is that the computation of the inverse matrices

$\tilde{S}^{-1}_{i+\frac{1}{2}}$ and $\tilde{C}^{-1}_{i+\frac{1}{2}}$ is exact and removes the oscillations of the MacCormack scheme but requires about 30% more work per time step than the Steger-Warming splitting. Another advantage of the new scheme is that it unifies several types of flux splitting, which is helpful when changing schemes. The Steger-Warming splitting is obtained using $D = \mathrm{diag}(1,1,1,1)$ for the positive flux vector and $D = \mathrm{diag}(0,0,0,0)$ for the negative flux vector. The MacCormack splitting is obtained by using at odd time intervals $D = \mathrm{diag}(1,1,1,1)$ and $D = \mathrm{diag}(0,1,1,0)$ and at even time intervals $D = \mathrm{diag}(1,0,0,1)$ and $D = \mathrm{diag}(0,0,0,0)$ for the positive and negative flux vectors respectively. More details can be found in Van der Vegt (1991).

Linearization

The flux vectors defined in the previous section are all non-linear functions of $\mathbf{U}$, so in order to solve the set of non-linear equations (3) implicitly, they have to be linearized around their value at time $t = t_n$. This is a delicate procedure if time accuracy is to be maintained. If only a steady state solution is needed, one can use the Steger-Warming splitting for the implicit part, but this adds a significant error when time accuracy is important. Due to the averaging process, the flux vector at surface $i + \frac{1}{2}$ is a function of both $\mathbf{U}_i$ and $\mathbf{U}_{i+1}$:

$$\Delta\hat{\mathbf{E}}^{\pm}(\mathbf{U}_i, \mathbf{U}_{i+1}) \cong \frac{\partial\hat{\mathbf{E}}^{\pm}}{\partial\mathbf{U}_i}\Delta\mathbf{U}_i + \frac{\partial\hat{\mathbf{E}}^{\pm}}{\partial\mathbf{U}_{i+1}}\Delta\mathbf{U}_{i+1}$$

with similar linearization for the vector $\Delta\mathbf{G}^n$. Analogously we have to linearize the viscous terms:

$$\Delta\hat{\mathbf{V}}^n_{vis_\xi}(\mathbf{U}) \cong \frac{\partial\hat{\mathbf{V}}^n_{vis_\xi}}{\partial\mathbf{U}}\Delta\mathbf{U}^n + \frac{\partial\hat{\mathbf{V}}^n_{vis_\xi}}{\partial\mathbf{U}_\xi}\Delta\mathbf{U}^n_\xi + \frac{\partial\hat{\mathbf{V}}^n_{vis_\xi}}{\partial\mathbf{U}_\eta}\Delta\mathbf{U}^n_\eta$$

A similar linearization is used for $\Delta\hat{\mathbf{V}}^n_{vis_\eta}$. The suffices + and − on the Jacobian matrices of the inviscid flux vectors refer to the components corresponding to positive and negative eigenvalues. In order to maintain time accuracy, none of the components in the matrices obtained by linearization should be neglected; this is not possible with approximate factorization. However, this greatly increases the difficulty of solving the linear system of equations, as discussed in the next section. Careful linearization is important because it greatly extends the stability limit of the scheme. If, for instance, the homogeneity property is used to linearize the inviscid flux vectors $\mathbf{E}$ and $\mathbf{G}$ then, in many cases, the time step can not be much larger than the time step for an explicit scheme.

Iterative Solution of Matrix Equation

After discretization, a system of linear algebraic equations is obtained:

$$\hat{A}^n_{ij}\Delta\mathbf{U}^n_{i,j} + \hat{B}^n_{ij}\Delta\mathbf{U}^n_{i,j+1} + \hat{C}^n_{ij}\Delta\mathbf{U}^n_{i,j-1} + \hat{D}^n_{ij}\Delta\mathbf{U}^n_{i+1,j} + \hat{E}^n_{ij}\Delta\mathbf{U}^n_{i-1,j} +$$

$$\hat{F}^n_{ij}\Delta\mathbf{U}^n_{i+1,j+1} + \hat{G}^n_{ij}\Delta\mathbf{U}^n_{i-1,j+1} + \hat{H}^n_{ij}\Delta\mathbf{U}^n_{i+1,j-1} + \hat{I}^n_{ij}\Delta\mathbf{U}^n_{i-1,j-1} = \hat{\mathbf{R}}^n_{ij}$$

Here $\hat{A}^n_{ij}, \cdots, \hat{I}^n_{ij}$ represent the Jacobian matrices obtained by linearizing the flux vectors and $\mathbf{R}^n_{ij}$ is the right-hand side. For the compressible Navier-Stokes equations in two dimensions, they are 4×4 matrices.

Solution of this system is a time consuming part of the algorithm, taking about 30% of the total time. The use of flux splitting for the non-linear terms makes the matrices diagonally dominant and allows use of iterative methods. Gauss-Seidel line relaxation in the streamwise direction reduces the block nona-diagonal matrix to a block tri-diagonal matrix. The block tri-diagonal matrix is solved by direct inversion. If a steady flow is being computed, it is not necessary to iterate the Gauss-Seidel line relaxation to convergence at each time step, but for time-accurate solutions, convergence to accuracy smaller than the truncation error is required. Direct inversion may become then prohibitively expensive. An alternative must be found. Dexun *et al.* (1989) suggested that using LU decomposition of abridged matrices, consisting of the main diagonals of the block tri-diagonal matrices, as a preconditioner and solving the block tri-diagonal matrices iteratively gives a significant improvement. It is convergent for moderate time steps, fully vectorizable, and gives a significant reduction in computing time. The full iterative scheme so obtained converges very rapidly. Dexun *et al.* (1989) only used two iterations for a steady state problem. Machine accuracy is obtained in two to four Gauss-Seidel sweeps. The inner iteration, used to invert the block tri-diagonal matrices within each Gauss-Seidel sweep, converges in about ten to fifteen iterations for the first sweep and one to four iterations for the following inner iterations. Residual correction and under- or over-relaxation were tried out and did not improve the convergence rate. If a steady state solution is required, solving the block tridiagonal matrices with a direct method allows a significantly larger time step.

Boundary Conditions

Outflow boundary conditions within the boundary layer present problems. The main trouble is in the subsonic region close to the wall. Setting the pressure in this region to the free-stream pressure does not work because it creates instabilities whenever the pressure becomes smaller than the free-stream pressure. The outflow boundary conditions adopted are zeroth order extrapolation, which performed well and had no noticeable upstream influence. For some applications, this condition is not suitable because it is reflective. The boundary conditions at the solid surface also require special attention. For an adiabatic wall, the conditions were zero velocity and heat flux at the wall, determination of the pressure from the equation of state, and use of the continuity and energy equations to close the system. For an isothermal wall, the temperature was fixed and only the continuity equation was used to close the system. The conditions are implemented using a half cell at the solid wall, as discussed in Vinokur (1989), and works very well. Conditions such as zero normal pressure gradient and/or zero density gradient are not valid at the wall in a viscous fluid and should not be used. In regions with nearly inviscid flow, characteristic boundary conditions are used which minimize reflections, for more detail see Giles (1988).

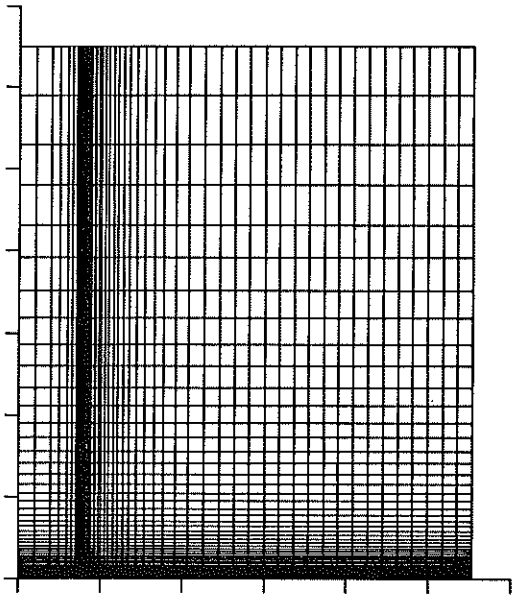

FIGURE 1. Grid for calculation of flow field above flat plate.

Boundary Layer on a Finite Flat Plate

Careful testing has been performed to investigate the accuracy of the numerical scheme. The first test case was the flow about an adiabatic flat plate at zero angle of incidence. Results were compared with the analytically derived results of Crocco (1941); see also Schlichting (1979). The Mach number was 2 and Prandtl number, 1. The viscosity law $\mu = T$ was used in order to enable comparison with the results of Crocco. All quantities are non-dimensionalized with their free-stream values and plate length. In order to test the ability of the model to compute shocks, the case of a finite plate in a uniform flow was considered and the results at the trailing edge were compared with Crocco. This removed the problem of choosing an inflow profile. Because the x- and y-derivatives are equally important at the nose of the plate, it is necessary to use small square grid cells in this region, see Fig. 1, while strong grid stretching is required in the boundary layer region further downstream. If the grid is stretched too much in one direction at the nose, the computations diverge. In Fig. 2 and 3, the Steger-Warming and MacCormack splittings on a 100×100 grid are compared with the results of Crocco. It is clear that the MacCormack splitting gives much better results; the Steger-Warming splitting is much too dissipative in the boundary layer. It must be remarked, however, that the Steger-Warming splitting does not perform as badly as claimed by MacCormack *et al.* (1989) for the Blasius boundary layer. The small deviations from the Crocco results must be attributed to the effects of the shock.

The second test case was the same flat plate but with an isothermal wall and Prandtl number .7. The general features of the flow field are presented in Fig. 4, which shows the density field at steady state. There is a large density jump at the

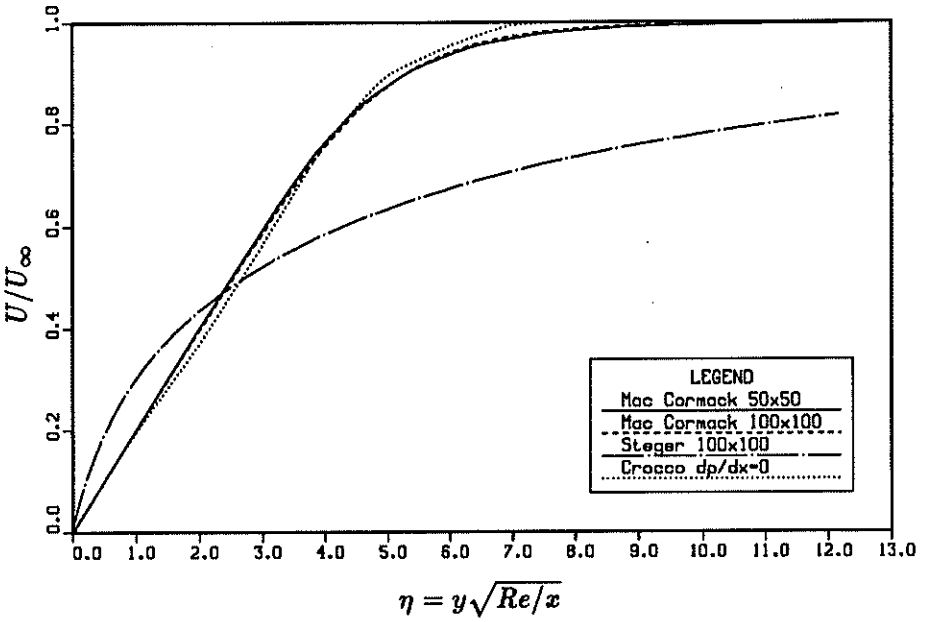

FIGURE 2. Velocity profile in flat plate boundary layer with adiabatic wall. Mach = 2, Pr=1, Re=530000.

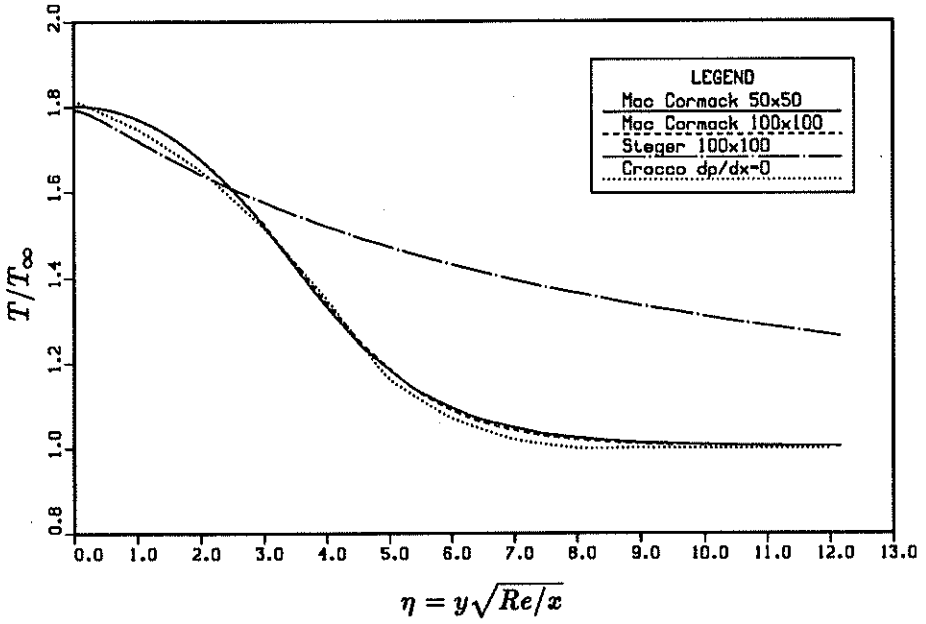

FIGURE 3. Temperature profile in flat plate boundary layer with adiabatic wall. Mach = 2, Pr=1, Re=530000.

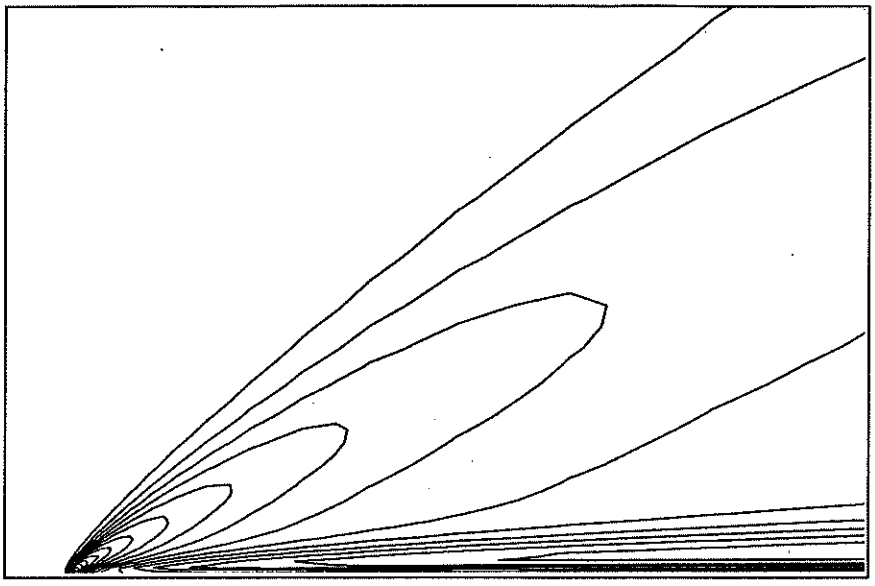

FIGURE 4. Density contours at nose of isothermal flat plate. Mach = 2, Pr=.7, Re=530000.

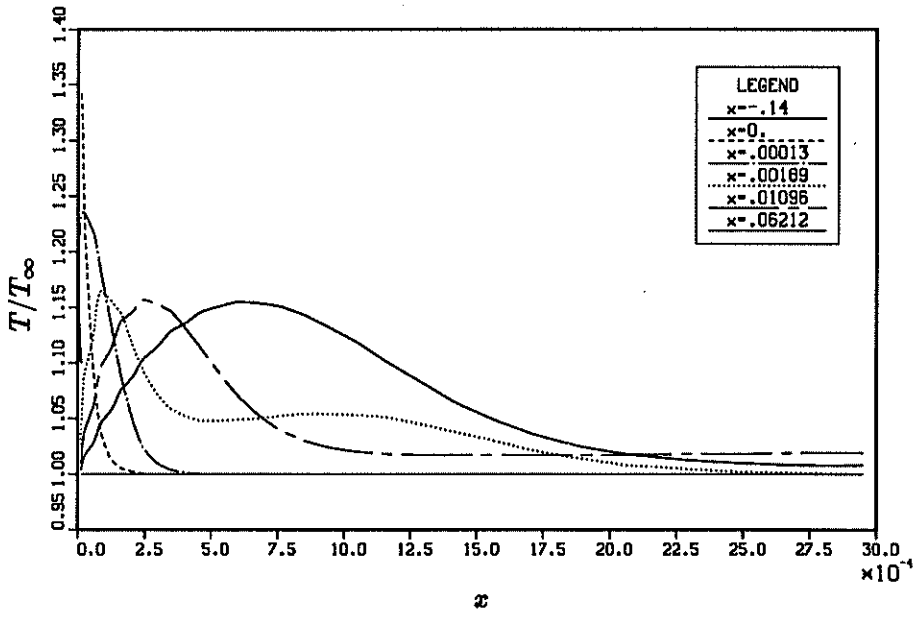

FIGURE 5. Temperature profile at nose of isothermal flat plate. Mach = 2, Pr=.7, Re=530000.

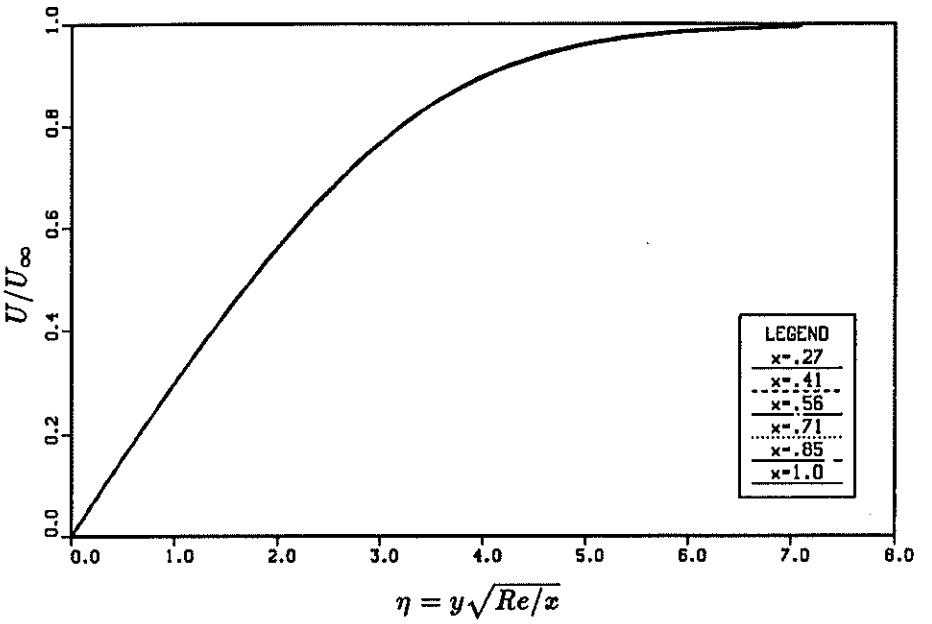

FIGURE 6. Velocity profile at different stations in flat plate boundary layer with isothermal wall. Mach = 2, Pr=.7, Re=530000.

nose of the plate, followed by expansion around the outer edge of the boundary layer; a weak shock originates from the nose of the plate. After the nose region, the flow relaxes to a boundary layer. Fig. 5 shows how fast the temperature profile relaxes from the nose to the boundary layer profile. The rapid change puts severe demands on the numerical scheme. In order to test the outflow boundary conditions and to see how well the similarity laws are satisfied, the velocity and temperature profiles at several downstream locations are plotted in Fig. 6 and 7. The plots show that the similarity law is very well satisfied, even at x=1, the last grid point on the plate, so there are no noticeable effects of outflow boundary conditions, even in the subsonic region. The results also compare well with those obtained by Hantzsche *et al.*; see also Schlichting (1979). Good agreement with the similarity profile was also obtained for the adiabatic flat plate at Mach=2.

The third test case is the flat plate with adiabatic wall, Mach number 5 and Prandtl number 1. This is a much more severe case due to the rapid changes at the nose of the plate. Fig. 8 and 9 show the velocity and temperature profiles at various downstream locations plotted against the similarity parameter η. The temperature rise is now as large as a factor of six in the boundary layer and much higher at the nose. The boundary layer is much thicker than in the Mach 2 cases due to heating. Another problem is the definition of the initial field. The computations for $M = 2$ were started from a uniform flow field, but at higher Mach numbers, the converged Mach 2 result was used as initial field.

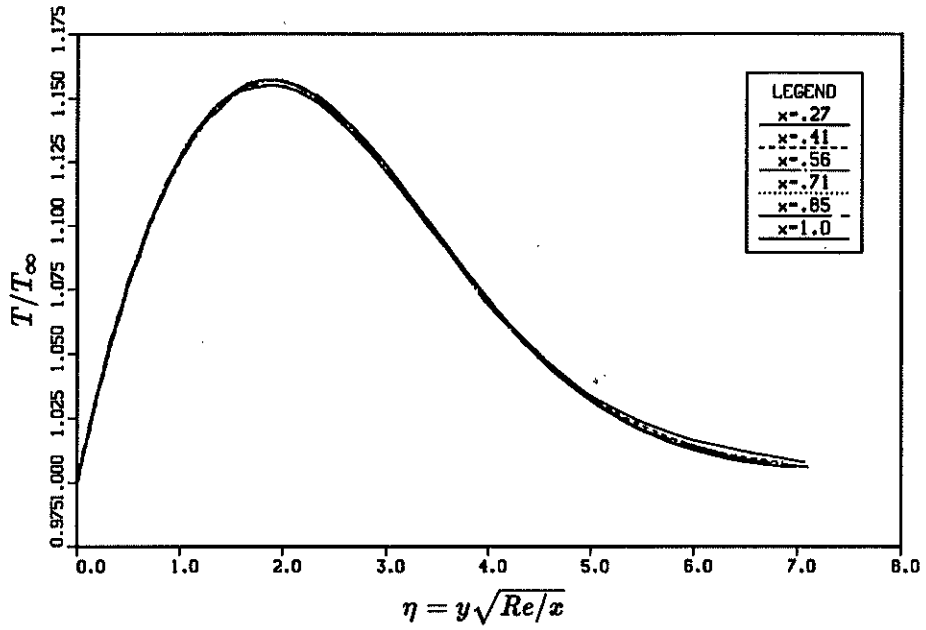

FIGURE 7. Temperature profile at different stations in flat plate boundary layer with isothermal wall. Mach = 2, Pr=.7, Re=530000.

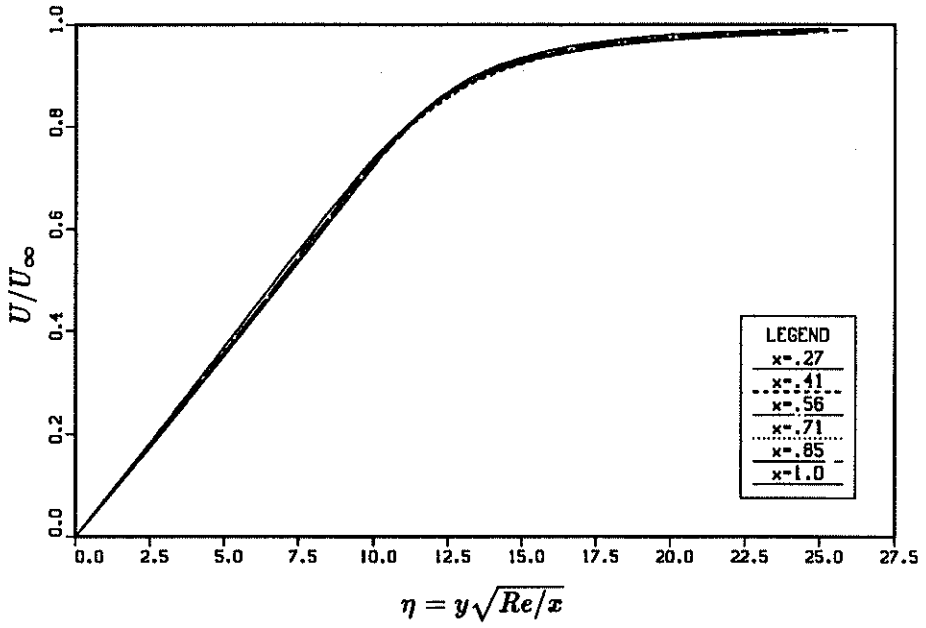

FIGURE 8. Velocity profile at different stations in flat plate boundary layer with adiabatic wall. Mach = 5, Pr=1, Re=530000.

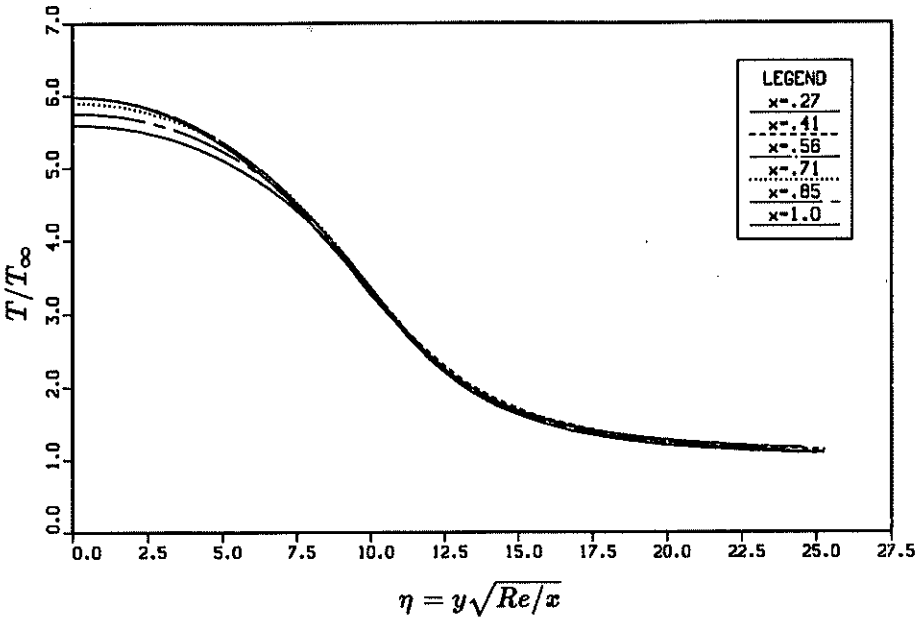

FIGURE 9. Temperature profile at different stations in flat plate boundary layer with adiabatic wall. Mach = 5, Pr=1, Re=530000.

Second Mode Instability in a Flat Plate Boundary Layer at Mach 4.5

Calculations are currently being done on the transition in a flat plate boundary boundary layer with an adiabatic wall at a Mach number 4.5. This case has been studied by Erlebacher and Hussaini (1990), (E&H), with a spectral code and is a severe test case of a finite-volume code because a spectral code is better suited to this problem. The stability calculations investigate the temporal stability of the second mode in the flat plate boundary layer. The existence of multiple unstable modes at high Mach numbers is a feature not found in low Mach number flows. For a review of compressible stability theory see Mack (1984). The appearance of multiple unstable modes starts at a Mach number of approximately 2.2. The purpose of the direct simulations is to study the effect of wall boundary conditions on flow stability. It turns out that the first mode is stabilized by wall cooling, which was discovered by Lees and Lin (1946), but the second mode is destabilized by wall cooling; for a detailed discussion see Mack (1984). Another motivation for studying the second mode is that two-dimensional waves are the most unstable second modes. The simulations are temporal, so the boundary layer is assumed to be parallel and periodic along the flat plate. The initial perturbations are of the form:

$$u'(x,y,t) = \hat{u}(y)e^{i(\alpha x - \omega_r t) + \omega_i t}$$

so ω_r is the frequency and ω_i is the growth rate. In order to prevent the boundary layer from growing, source terms are added to the right-hand side of the Navier-Stokes equations to cancel the terms which would create a non-zero vertical velocity

in the laminar flow. With this modification, the mean flow remains the constant mean flow used in the stability calculations, which generate the initial disturbances for the direct simulation. These disturbances are now added to the mean flow profile.

Linear stability calculations were made using the Cosal code of Malik (1982) for the case done by E&H. Identical results were obtained for the first mode, but for the second mode the results were slightly different. We used the parameters $M_\infty = 4.5$, $Re_{\delta^*} = 8000$, $\alpha = 2.25$, $Pr = .7$, and Sutherlands viscosity law. All parameters are non-dimensionalized using the displacement thickness δ^* and free stream values. The growth rate obtained from Cosal was: $\omega = 2.04706 + .02283i$, whereas E&H obtained $2.04674 + .02149i$, using a spectral code. Their Reynolds number was reported incorrectly as $Re_{\delta^*} = 10000$ instead of $Re_{\delta^*} = 8000$. It was decided to test the convergence of the eigenvalue computation with Cosal and use this result in the direct simulation. Table 1 shows the results of the growth rate for various numbers of grid points:

npoint	ω_r	ω_i
250	2.047045514267	.02294520289382
500	2.047060523908	.02285383626108
750	2.047063145850	.02283708143864
1000	2.047064045772	.02283124312681
1250	2.047064484897	.02282849820898
1500	2.047064741600	.02282702318168

Table 1. Convergence History of Eigenvalue Calculation for Flat Plate, $M_\infty = 4.5$, $Pr = .7$, $Re_{\delta^*} = 8000$.

This table shows that a large number of grid points is needed. This can be partly attributed to inefficiencies in the Cosal code, which is currently being improved, and to the steep gradients in the eigenfunctions; see Figures [10]-[13].

Using these as initial profiles pointed out several problems in direct simulations of transition. The two main problems are the boundary conditions far from the flat plate and providing enough resolution at the right places. At the top surface, non-reflecting characteristic boundary conditions based on inviscid flow are imposed. If reflecting boundary conditions are being used, as in E&H, the reflections influence the transition after some time. The problem with the non-reflecting boundary conditions is that they enforce zero mean vertical velocity, which is unphysical. The zero vertical velocity makes the top wall a characteristic surface for the mean flow and does not allow imposition of boundary conditions. Most theories for non-reflecting boundary conditions assume small disturbances around some mean value, but this becomes a singular case in our situation. The alternative, linearizing about the eigenfunctions, does not work either because this creates local inflow and outflow which change in time. These boundary conditions allow information to travel from infinity into the boundary layer, which is unphysical. It was finally decided to impose outflow everywhere on the top surface because this reflects most closely the

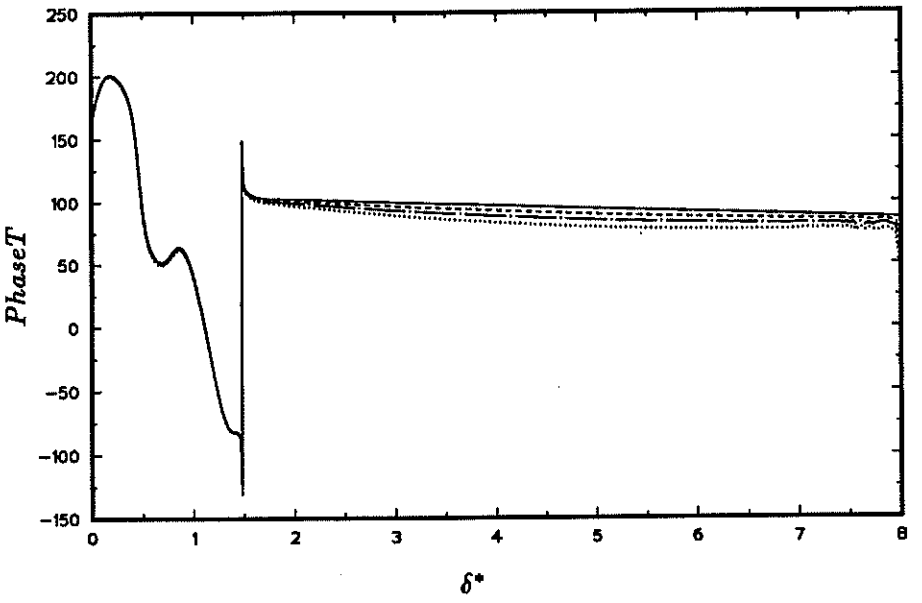

FIGURE 10. Phase of Temperature Disturbances in Flat Plate Boundary Layer. $M_\infty = 4.5$, $Pr = .7$, $Re_{\delta^*} = 8000$.

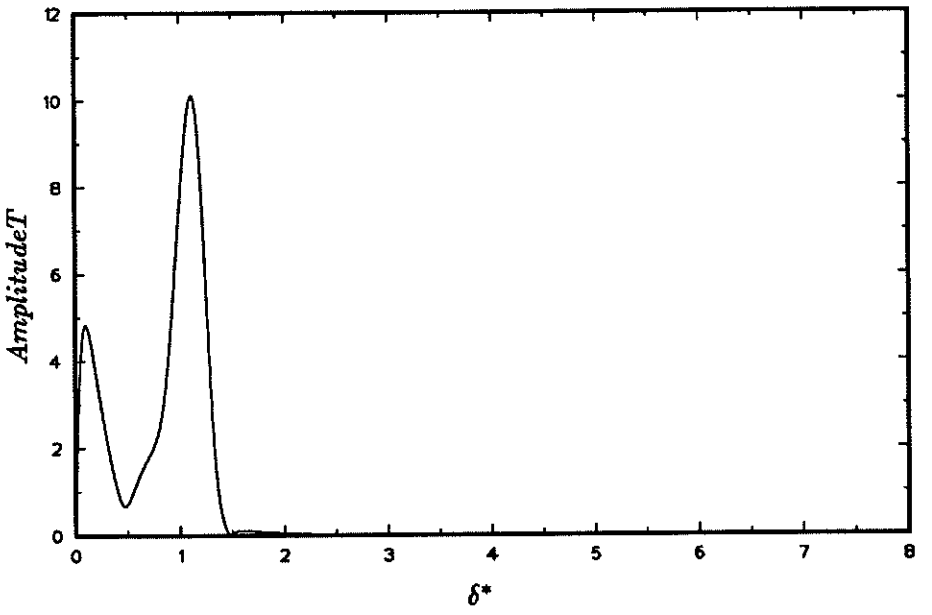

FIGURE 11. Amplitude of Temperature Disturbances in Flat Plate Boundary Layer. $M_\infty = 4.5$, $Pr = .7$, $Re_{\delta^*} = 8000$.

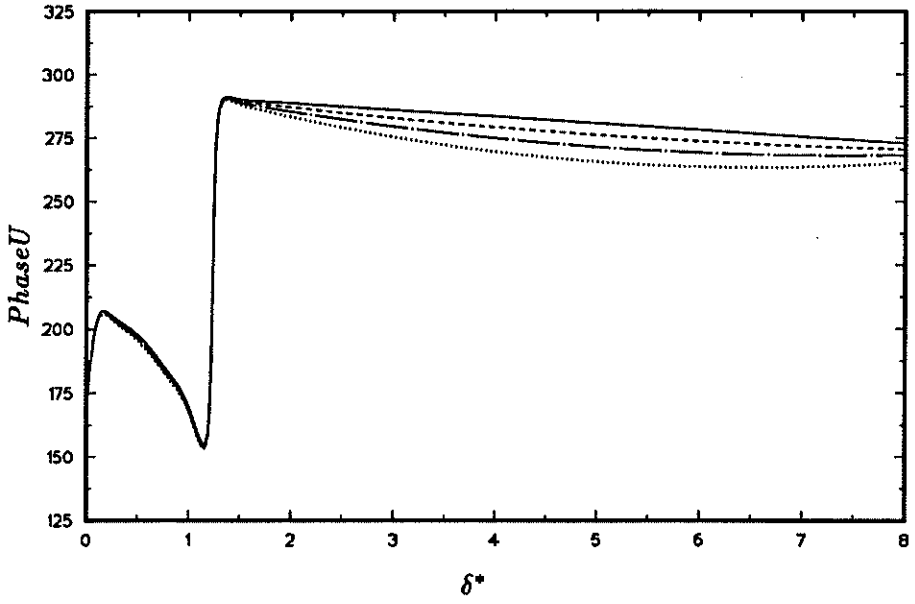

FIGURE 12. Phase of Velocity Disturbances in Flat Plate Boundary Layer. $M_\infty = 4.5$, $Pr = .7$, $Re_{\delta^*} = 8000$.

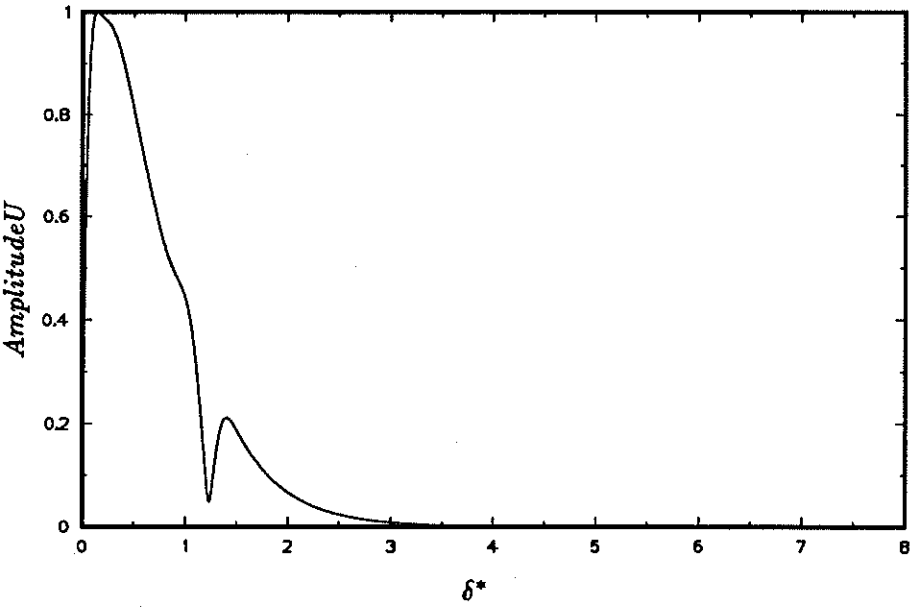

FIGURE 13. Amplitude of Velocity Disturbances in Flat Plate Boundary Layer. $M_\infty = 4.5$, $Pr = .7$, $Re_{\delta^*} = 8000$.

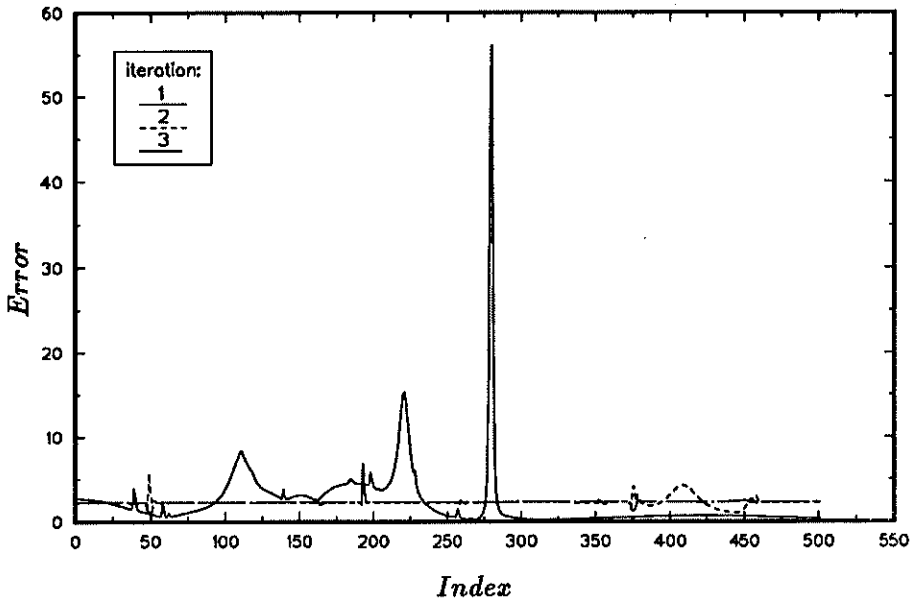

FIGURE 14. Local Error in Flat Plate Calculations at Different Grid Points. $M_\infty = 4.5$, $Pr = .7$, $Re_{\delta^*} = 8000$.

physical processes. This removed oscillations between the critical layer and the top wall, although some small oscillations are still visible in the temperature phase angle at the top wall, Fig. [10].

Figures [10] to [13] show the amplitudes and phases of the disturbances of temperature and velocity at several time steps. The initial disturbances are the eigenfunctions obtained from the linear stability code, with amplitude 2% of the free steam velocity. The number of grid points for this calculation was 128x500, with grid stretching outside the boundary layer. The results do not show strong numerical oscillations. The phase angle shows that the flow field is changing, although not clearly visible, the amplitudes also grow.

Unfortunately, problems remain. One is that it takes a long time for the disturbances to start growing. This can be attributed to small numerical errors in the eigenfunctions obtained from the linear stability code; they slightly differ from the eigenfunctions of the most unstable mode. Lack of resolution in some parts of the flow field also contributes to a slower growth through numerical diffusion. In order to improve the accuracy, it was decided to implement an adaptive grid method. For a general review of these methods, see Thompson (1985). The adaptive grid scheme tries to generate a grid which has a uniform error in computational space; the control parameters are the gradient and radius of curvature. Figure [14] shows that three iterations greatly reduce the error and make it more uniform. The original grid did not have enough points, especially in the temperature critical layer, which becomes clear comparing the original grid and the modified one in Figure [15]. For transition calculations, this region is dominant because the temperature

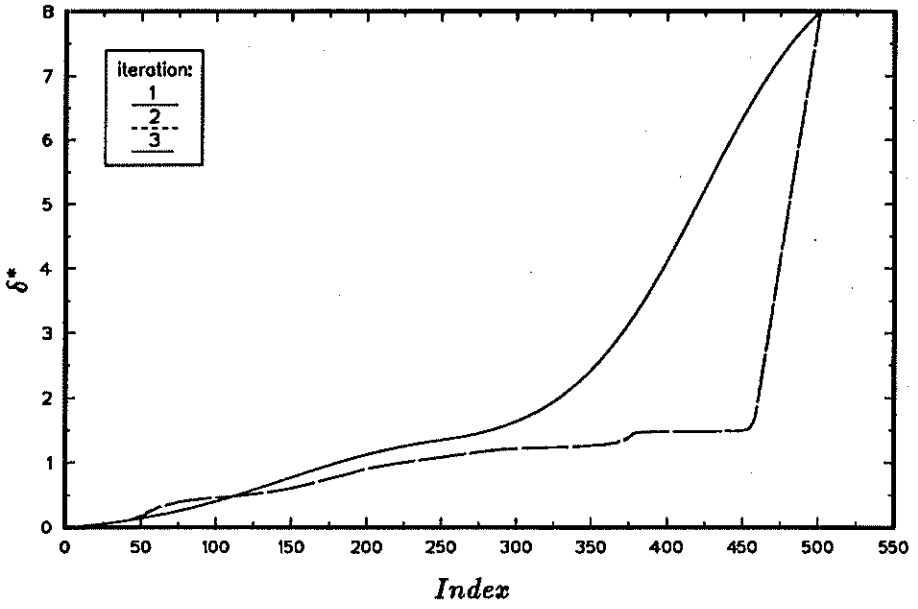

FIGURE 15. Grid for Flat Plate Calculations. $M_\infty = 4.5$, $Pr = .7$, $Re_{\delta^*} = 8000$.

fluctuations are the largest in the flow field. The simulations are currently being repeated using the adaptive grid scheme. Improvements in the linear stability code are also being pursued.

3. Work to be done

- Continue simulations of temporal stability of second mode for a flat plate with different temperature boundary conditions.
- Improvement of non-reflecting boundary conditions to be able to study spatial stability on a flat plate and a wedge.
- Continue activities to transform code to solve three-dimensional flows.
- Study of stability of a shock layer perturbed by sound waves.

Acknowledgement

Thanks are due to Dr. G. Erlebacher for providing the linear stability code.

REFERENCES

BEAM, R. M. & WARMING, R. F. 1978 An Implicit Factored Scheme for the Compressible Navier-Stokes Equations. *AIAA Journal.* **16**, No 4, 393-402.

CROCCO, L. 1941 Sullo Strato Limite Laminare Nei Gas Lungo Una Lamina Piana, Rendiconti di Matematica delle sue Applicazioni, University Rome, 139-152.

DEXUN, F. & YANWEN, M. 1989 On Efficiency and Accuracy of Numerical Methods for Solving Aerodynamic Equations, Symposium Tokyo.

ERLEBACHER, G. & HUSSAINI, M. Y. 1990 Numerical Experiments in Supersonic Boundary-Layer Stability. *Physics of Fluids.* **A2**, 94-104.

GILES, M. 1988 Non-Reflecting Boundary Conditions for the Euler Equations. *Report MIT CFDL-TR-88-1.*

HANTZSCHE, W. & WENDT, H. 1940 Zum Kompressibilitätseinfluss bei der Laminaren Grenzschicht der Ebenen Platte. *Jahrbuch Deutsche Luftfahrtforschung.* **I**, 517-521.

LEES, L. & LIN, C. C. 1946 Investigation of the Stability of the Laminar Boundary-Layer in a Compressible Fluid. *NACA Technical Note 1115.*

MACCORMACK, R. W. & CANDLER, G. V. 1989 The Solution of the Navier-Stokes Equations using Gauss-Seidel Line Relaxation. *Computers and Fluids.* **17**, 135-150.

MACK, L. M. 1984 Special Course on Stability and Transition of Laminar Flow. *AGARD Report 709.*

MALIK, M. R. 1982 Finite-Difference Solution of the Compressible Stability Eigenvalue Problem. *Nasa Contracter Report NAS1-16572.*

SCHLICHTING, H. 1979 Boundary Layer Theory, Mc Graw-Hill.

STEGER, J. L. & WARMING, R. F. 1981 Flux-Vector Splitting of the Inviscid Gasdynamic Equations with Application to Finite- Difference Methods. *Journal of Computational Physics.* **40**, 263-293.

THOMPSON, J. T., WARSI, Z. U. A. & MASTIN, C. W. Numerical Grid Generation 1985 North-Holland.

VAN DER VEGT, J. J. W. 1991 Assessment of Flux Vector Splitting for Viscous Compressible Flows. *AIAA Paper 91-0243.* 29th Aerospace Sciences Meeting and Exhibit, Reno, Nevada.

VINOKUR, M. 1989 An Analysis of Finite-Difference and Finite-Volume Formulations of Conservation Laws. *Journal of Computational Physics.* **81**, 1-52.